

A new cavity based absorption instrument for detection of water isotopologues in the upper troposphere and lower stratosphere

David S. Sayres, E. J. Moyer, T. F. Hanisco, J. M. St. Clair, F. N. Keutsch, A. O'Brien, N. T. Allen, L. Lapson, J. N. Demusz, M. Rivero, T. Martin, M. Greenberg, C. Tuozzolo, G. S. Engel, J. H. Kroll, J. B. Paul, and J. G. Anderson

Citation: [Review of Scientific Instruments](#) **80**, 044102 (2009); doi: 10.1063/1.3117349

View online: <http://dx.doi.org/10.1063/1.3117349>

View Table of Contents: <http://scitation.aip.org/content/aip/journal/rsi/80/4?ver=pdfcov>

Published by the [AIP Publishing](#)

Articles you may be interested in

[A new direct absorption tunable diode laser spectrometer for high precision measurement of water vapor in the upper troposphere and lower stratosphere](#)

Rev. Sci. Instrum. **84**, 074102 (2013); 10.1063/1.4815828

[A new photolysis laser-induced fluorescence instrument for the detection of H₂O and HDO in the lower stratosphere](#)

Rev. Sci. Instrum. **79**, 064101 (2008); 10.1063/1.2940221

[Lightweight dew-/frost-point hygrometer based on a surface-acoustic-wave sensor for balloon-borne atmospheric water vapor profile sounding](#)

Rev. Sci. Instrum. **77**, 014502 (2006); 10.1063/1.2140275

[A fast-response chemical ionization mass spectrometer for in situ measurements of HNO₃ in the upper troposphere and lower stratosphere](#)

Rev. Sci. Instrum. **71**, 3886 (2000); 10.1063/1.1289679

[Plume processing of jet engine exhaust aerosols injected into the upper troposphere and lower stratosphere](#)

AIP Conf. Proc. **534**, 693 (2000); 10.1063/1.1361959



Discover the IQ-2000—
A new way to
INSPIRE.

Visit us at Pittcon and ACS.

 **Extrel**
Core Mass Spectrometers

A new cavity based absorption instrument for detection of water isotopologues in the upper troposphere and lower stratosphere

David S. Sayres,^{a)} E. J. Moyer,^{b)} T. F. Hanisco, J. M. St. Clair,^{c)} F. N. Keutsch,^{d)} A. O'Brien, N. T. Allen, L. Lapson, J. N. Demusz, M. Rivero, T. Martin, M. Greenberg, C. Tuozzolo, G. S. Engel,^{e)} J. H. Kroll,^{f)} J. B. Paul,^{g)} and J. G. Anderson

Department of Earth and Planetary Sciences and Department of Chemistry and Chemical Biology, Harvard University, Cambridge, Massachusetts 02138, USA

(Received 19 January 2009; accepted 21 March 2009; published online 23 April 2009)

We describe here the Harvard integrated cavity output spectroscopy (ICOS) isotope instrument, a mid-IR infrared spectrometer using ICOS to make *in situ* measurements of the primary isotopologues of water vapor (H_2O , HDO, and H_2^{18}O) in the upper troposphere and lower stratosphere (UTLS). The long path length provided by ICOS provides the sensitivity and accuracy necessary to measure these or other trace atmospheric species at concentrations in the ppbv range. The Harvard ICOS isotope instrument has been integrated onto NASA's WB-57 high-altitude research aircraft and to date has flown successfully in four field campaigns from winter 2004–2005 to the present. Off-axis alignment and a fully passive cavity ensure maximum robustness against the vibrationally hostile aircraft environment. The very simple instrument design permitted by off-axis ICOS is also helpful in minimizing contamination necessary for accurate measurements in the dry UTLS region. The instrument is calibrated in the laboratory via two separate water addition systems and crosscalibrated against other instruments. Calibrations have established an accuracy of 5% for all species. The instrument has demonstrated measurement precision of 0.14 ppmv, 0.10 ppbv, and 0.16 ppbv in 4 s averages for H_2O , HDO, and H_2^{18}O , respectively. At a water vapor mixing ratio of 5 ppmv the isotopologue ratio precision is 50‰ and 30‰ for δD and $\delta^{18}\text{O}$, respectively. © 2009 American Institute of Physics. [DOI: 10.1063/1.3117349]

I. INTRODUCTION

Water vapor is the dominant greenhouse gas in the atmosphere, and the vertical and latitudinal distribution of water vapor, as well as the partitioning between vapor and condensate, plays a major role in setting the radiative balance of the atmosphere. Increases in the water vapor mixing ratio of the stratosphere would accelerate catalytic ozone loss,^{1,2} and changes in upper tropospheric water vapor, on a per molecule basis, are the single strongest factor in altering radiative forcing.^{3–5} These water vapor feedbacks, along with changes in condensed-phase water in the form of clouds, are the largest source of uncertainty in predictions of future climate.^{6,7} Given the radiative and chemical importance of water vapor, accurate forecasts by global climate models will require a deeper understanding of how water vapor will

change as the result of changes in radiative forcing by carbon dioxide and methane resulting from primary energy generation.

Numerous mechanisms have been proposed to explain the water vapor mixing ratios observed in the tropical upper troposphere and stratosphere: (1) *in situ* dehydration either via large-scale ascent or by advection above cold convective anvils;^{8,9} (2) dehydration from deep convection that mixes dry convective outflow with moister air;^{10–12} and (3) convective hydration in which deep convection lofts ice into under-saturated air.^{13,14} The ratio of water vapor isotopologues is a tracer of processes that cause a phase change in water, and therefore measurements of water isotopologues can quantitatively differentiate between these various mechanisms.^{15,16} During condensation, the heavier isotopologue is partitioned preferentially into the condensed phase. Therefore, as water condenses and the ice is removed, the remaining water vapor is isotopically lighter than the initial water vapor. Isotope ratios are typically written as the ratio of the heavier isotope (e.g., HDO or H_2^{18}O) to the more abundant lighter isotope (H_2O) referenced to a standard, in the case of water, Vienna Standard Mean Ocean Water (VSMOW), which has a $[\text{HDO}]/[\text{H}_2\text{O}]$ ratio of 3.115×10^{-4} .¹⁷ Deviations from the standard δ are reported in parts per thousand (‰) using Eq. (1),

$$\delta\text{D} = \left[\frac{(\text{HDO}/\text{H}_2\text{O})_{\text{sample}}}{(\text{HDO}/\text{H}_2\text{O})_{\text{VSMOW}}} - 1 \right] 1000. \quad (1)$$

^{a)}Electronic mail: sayres@huarp.harvard.edu.

^{b)}Present address: Department of Geophysical Sciences, University of Chicago, Chicago, IL.

^{c)}Present address: Geology and Planetary Sciences Division, California Institute of Technology, Pasadena, CA.

^{d)}Present address: Department of Chemistry, University of Wisconsin, Madison, WI.

^{e)}Present address: Department of Chemistry, University of Chicago, Chicago, IL.

^{f)}Present address: Department of Civil and Environmental Engineering, Massachusetts Institute of Technology, Cambridge, MA.

^{g)}Present address: Novawave Technologies, Redwood City, CA.

Traditional absorption techniques using a Herriott cell and tunable diode lasers lack both the sensitivity and accuracy necessary to simultaneously measure both water vapor and its less abundant isotopologues, which have typical concentrations in the upper troposphere and lower stratosphere (UTLS) on the order of 3 ppmv, 300 pptv, and 5 ppbv for H₂O, HDO, and H₂¹⁸O, respectively, and values of δD and $\delta^{18}O$ of $-600‰$ and $-150‰$, respectively. In order to measure the isotopic ratio to within 20‰, H₂O, HDO, and H₂¹⁸O measurements must have uncertainties less than 0.2 ppmv, 20 pptv, and 120 pptv, respectively. The Harvard integrated cavity output spectroscopy (ICOS) isotope instrument, henceforth Harvard ICOS, leverages new electronic and laser technologies coupled with the sensitivity of cavity enhanced absorption spectroscopy to achieve the precision and accuracy necessary to provide scientifically relevant *in situ* measurements of extremely scarce trace gas species in the atmosphere. Like other cavity enhanced techniques such as cavity ringdown spectroscopy,¹⁸ the sensitivity of ICOS comes from coupling coherent light into a high-finesse optical cavity composed of two high-reflectivity mirrors. Light is trapped in the cavity for tens of microseconds, yielding kilometer path lengths in meter-length cells, typically an amplification of 5000 in path length. The ICOS technique differs from its precursors in that instead of monitoring the decay of light from a pulsed source, the steady state power emitted from the cavity is measured as the frequency of the laser is scanned. Changes in the steady state output power are due to intracavity losses from molecular absorption.^{19–21}

The Harvard ICOS instrument is designed for *in situ* sampling on high-altitude aircraft in the middle and UTLS and is currently configured to measure the four primary isotopologues of water (H₂O, HDO, H₂¹⁸O, and H₂¹⁷O) as well as methane (CH₄) in the mid-IR at 6.7 μ m. *In situ* airborne sampling requires fast time response, high accuracy and precision, and low contamination from the instrument inlet and plumbing. The Harvard instrument is able to measure water vapor from 1 ppmv to a few thousand ppmv, values typical of the middle and UTLS, as well as simultaneous measurements of the less abundant isotopologues. Making simultaneous measurements is essential since the concentrations of each species can vary rapidly, especially in areas near convective systems or sharp transition points between condensed phase and purely vapor phase zones. These rapid changes in water vapor (from tens to hundreds of ppmv in less than 100 meters or 0.5 s of flight time) require rapid sampling and data acquisition and short integration times. The acquisition rate reported here is a convolution of the data rate necessary to achieve the required precision and the rate at which the air is flushed through the instrument. In addition to these measurement considerations, the instrument must be robust enough to operate at temperatures as low as -80 °C and pressures as low as 60 hPa and be insensitive to vibrations intrinsic to the structure of the aircraft. Before discussing the details of the Harvard ICOS instrument, we review the theory behind the ICOS technique. A detailed understanding of the theory is necessary for maximizing the signal to noise and for accurately fitting the ICOS spectrum.

II. THEORY OF ICOS

The Harvard ICOS instrument uses a high-finesse optical cavity composed of two high-reflectivity mirrors ($R = 0.9998$) to trap light for approximately 14 μ s. The average amount of time that the light is trapped in the optical cavity or cavity time constant τ is dependent on the reflectivity of the mirrors R and the length of the cavity L as given by

$$\tau = \frac{L}{c(1-R)}. \quad (2)$$

If there is an absorber present inside the cavity then τ decreases and Eq. (2) is modified to account for the intracavity absorption,

$$\tau = \frac{L}{c[1-R+\alpha(\nu)]}, \quad (3)$$

where α is the frequency dependent absorption. In cavity ringdown spectroscopy, an absorption spectrum is produced by measuring τ as a function of laser frequency.²² In ICOS, light from a cw-laser is coupled into the optical cavity and the laser is scanned continuously. The intensity of light in the cavity is determined by the transmission of light through the mirror, the amount of time that the light is allowed to buildup in the cavity, and the loss of light through the two cavity mirrors or by molecular absorption. If the laser is scanned at a rate comparable to the cavity time constant, at any point in time there are multiple frequencies of light in the cavity, each decaying with their own time constant $\tau(\nu)$.

A physical model of the evolution of light in the cavity can be derived by writing the equation for the intensity of light inside the cavity as a function of time. The intensity of light that builds up in the cavity from time t' to time $t' + \Delta t$ is

$$\begin{aligned} I_{(t',t'+\Delta t)} &= \int_0^{\Delta t} P(t') T e^{-t/\tau(t')} dt \\ &= P(t') T \tau(t') [1 - e^{-\Delta t/\tau(t)}], \end{aligned} \quad (4)$$

where T is the transmission of the mirror and Δt is small enough so that the power emitted by the laser $P(t')$ and the decay time constant $\tau(t')$ can be assumed to be constant between times t' and $t' + \Delta t$. The terms before the brackets on the right hand side of the equation describe how much of the laser power gets transmitted into the cavity, and the exponential term accounts for the buildup or ring up of light. The intensity of light builds up with a characteristic time constant τ , as defined in Eq. (3).

Equation (4) only accounts for the buildup of light within the cavity. The intensity of light evolves in the cavity by ringing down over time as light is lost through the mirrors or by molecular absorption. Therefore, the intensity of light at some future point in time t is

$$I_{(t',t'+\Delta t)}(t) = P(t') T \tau(t') [1 - e^{-\Delta t/\tau(t')}] e^{-(t-t')/\tau(t')}. \quad (5)$$

This equation now fully accounts for the evolution of light that entered the cavity at a particular point in time t' , with both P and τ being dependent on when the light entered the cavity since the frequency of light is dependent on time. By summing Eq. (5) over all prior times we derive an equation

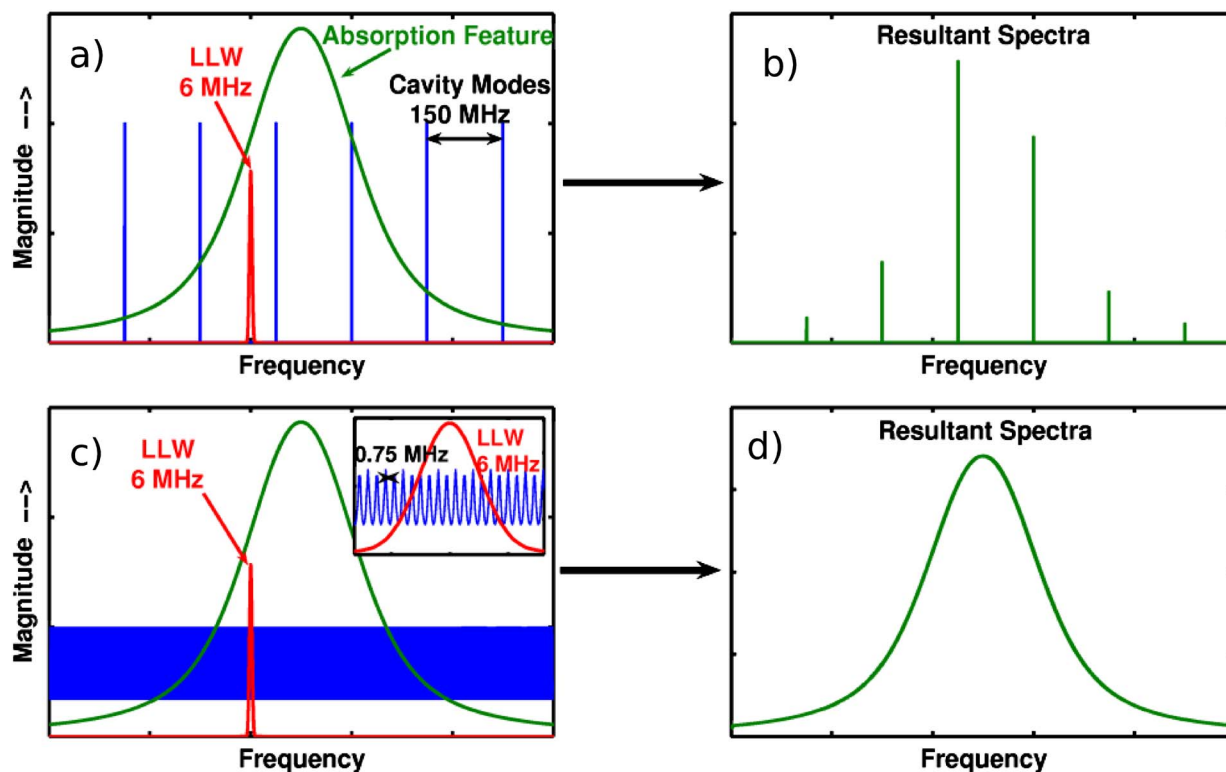


FIG. 2. (Color online) Plot a shows the spacing or FSR of the longitudinal cavity modes for a 90 cm cavity in blue. Also shown are the LLW and typical width of an absorption line. The LLW is narrow compared to the cavity mode spacing, resulting in large amplitude fluctuations whenever the frequency is resonant with one of these modes as shown in plot b. If the laser is aligned into the cavity to form a multipass pattern, then the cavity behaves like one that is n times longer. For a $n=200$ pass pattern the FSR of the cavity is reduced by 200 (plot c). The LLW is now broad compared to the FSR of the cavity (inset of plot c) but still narrow compared to an absorption line resulting in a smooth absorption feature as shown in plot d.

$$\theta = \arccos\left(1 - \frac{L}{R_m}\right). \quad (10)$$

For a spot pattern where the light becomes reentrant after 300 passes, there is some amount of overlap even after 27 passes (Fig. 3). Even this small amount of overlap will produce etalons. To reduce the magnitude of the cavity etalons further, the laser is scanned at a rate comparable with the cavity time constant. This shortens the amount of time that the resonant condition is met. However, if the laser is scanned too fast the molecular absorption features will also

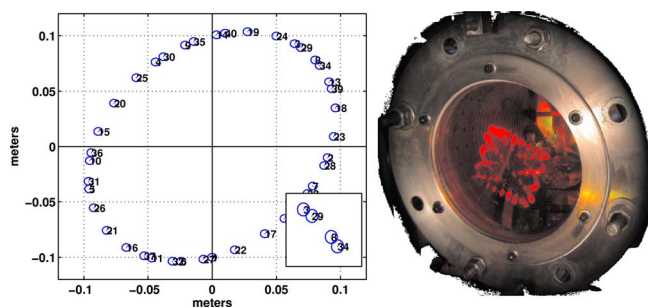


FIG. 3. (Color online) Calculated spot pattern for a cavity composed of spherical mirrors with a radius of curvature of 140 cm, cavity length of 90.57 cm, and for light of wavelength $6.7 \mu\text{m}$. Only the first 30 spots are shown. The light becomes re-entrant after 300 round trips. However, even after 27th pass there is some overlap between spots as shown in the enlarged portion of the figure. Pictured on the right is the spot pattern formed using a visible light. Due to slight astigmatism in the mirrors, the spots form a Lissajous pattern.

begin to blur. In practice, laser phase noise and mechanical instability leave spurious resonances as the major source of noise in the system.²⁷ If the cavity etalons are small enough they can be treated either as noise or fit as part of the baseline. The treatment of baseline etalons in the fitting algorithm is discussed in the data analysis section.

III. THE HARVARD ICOS ISOTOPE INSTRUMENT

The Harvard ICOS instrument is mounted in a pallet of NASA's WB-57 aircraft.²⁸ While it can fly in any of the four pallet positions it is preferable to fly as far forward (position 1) as possible to minimize contamination from the aircraft fuselage. It was mounted in the second position during engineering test flights in the winter of 2004–2005 and the TC4 (Ref. 29) campaign in the summer of 2007, in position 3 during the AVE-WIIF (Ref. 30) campaign in the summer of 2005, and in position one during the CR-AVE (Ref. 31) campaign in the winter of 2006. For the purposes of this discussion the instrument is divided into three main subsystems:

- (1) the laser and optical system, which includes the QCL, mercury cadmium telluride (MCT) detector, optical cavity, diagnostic etalon, and alignment mirrors;
- (2) the gas flow system including the inlet, distribution manifold, gas deck, and scroll pump; and
- (3) the data acquisition system including the QCL current (QCLI) driver, detector/preamp, and flight computer.

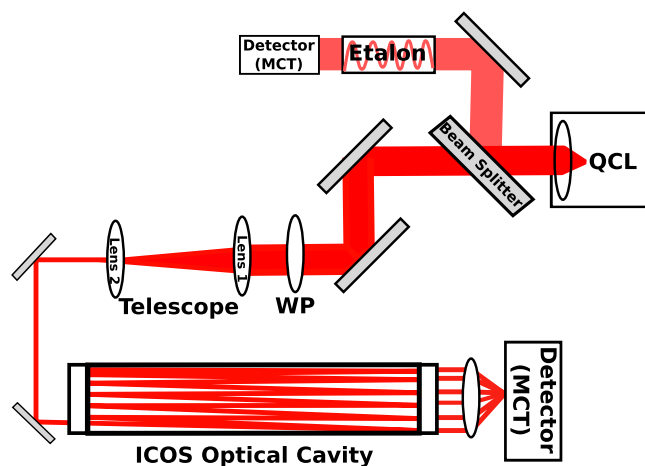


FIG. 4. (Color online) Schematic of the ICOS laser and optics system. The laser (QCL) is collimated by an internal lens and then passes through a beam splitter with a fraction diverted to a Ge-etalon used to reference the frequency scale. The majority of the light is focused via a telescope and steering mirrors into the ICOS optical cavity. The light transmitted through the rear mirror is focused onto the detector. Details of each component are discussed in the text.

A. Laser and optical system

The components comprising the laser and optical system are shown in Fig. 4. Light from a narrowband laser is focused through telescope optics and coupled into a high-finesse optical cavity, whose steady state output power is recorded by a detector. The tuning rate of the laser is simultaneously monitored by a diagnostic etalon. Due to the low transmission of the cavity mirrors only a small fraction of the laser light reaches the detector, necessitating the use of a high powered laser. The ICOS instrument uses a QCL developed by Alpes Lasers specifically for the purpose of atmospheric research. It produces 35 mW at $6.7 \mu\text{m}$ and can tune continuously between 1483 and 1489 cm^{-1} . In order to maintain cryogenic temperatures, a 4 L LN₂ dewar (Kadel) is used to house the QCL, which allows for 24 h of hold time, followed by 8 h of continuous use. This size dewar is large enough to allow for long duration flights and has enough nitrogen in case there is a delay in takeoff. The light from the QCL is collimated using a ZnSe lens (ISP Optics, part ZC-WW-24-4) located inside the dewar and mounted on the same copper block as the laser.

A germanium etalon is used to calibrate the frequency scale of the ICOS spectrum. An accurate, independent measure of the frequency scale is necessary because the tuning rate of the QCL is nonlinear in certain regions of the spectrum as can be seen in the bottom plot of Fig. 1. In addition, the frequency of light produced for a given current level drifts slightly as the laser warms up. A 3° wedged optic is used as a beam splitter (ISP Optics, part CF-WW3-50-5) and is located directly in front of the laser dewar. It allows 86% of the light to pass through, while 14% is diverted to the reference etalon. The etalon is a 6.3 cm piece of germanium with polished parallel faces coated for high-reflectivity at $6.7 \mu\text{m}$. The FSR of the etalon is 0.0198 cm^{-1} .

Following the beam splitter the light is aligned through a 1/4 waveplate (Fig. 4, labeled WP) and then into a focusing

telescope via a series of 2 in. silver coated steering mirrors (Newport, part 20D20ER.2). The 1/4 waveplate (Cleveland Crystals) acts to rotate the polarization of the laser beam in order to minimize feedback into the laser from reflections off of the cavity mirrors. As the QCL emits plane polarized light, a separate polarization stage is not needed. The telescope is comprised of two aspheric lenses (ISP Optics, part ZC-PM-25), with radii of curvature of 76 mm (lens 1) and 127 mm (lens 2) and are held in independent sliding mounts. This allows the position of the lenses to be easily changed depending on the radius of curvature of the cavity mirrors and the length of the cavity. After being focused by the telescope the laser beam is aligned into the optical cavity via two 1 in. silver coated alignment mirrors. The alignment mirror directly in front of the optical cavity can be moved parallel to the cavity mirror so that the laser beam can be directed into the cavity either on-axis or off-axis.

The optical cavity is comprised of a pair of 10 cm diameter mirrors mounted to the ends of an aluminum tube. The mirrors are composed of ZnSe with a radius of curvature of 140 cm and have antireflective coatings on the nonreflective side at 6.7 and $0.633 \mu\text{m}$ and high-reflectivity coatings on the curved surface of the mirror at the same wavelengths (coatings: Lohmstar Optics). The coatings at visible wavelengths allow for a red laser to be coaligned with the QCL for use in alignment. Due to slight astigmatism in the mirrors, the spots on the cavity mirrors form a Lissajous pattern as opposed to a typical Herriott spot pattern normally observed for spherical mirrors (Fig. 3). The mirrors are held by o-rings on their edge, and the mounts contain no alignment screws, which provides for a completely passive cavity. When aligning on-axis, it is advantageous to ensure that the mirrors are parallel and that the optical axis is coaligned with the mechanical center of the mirrors. Since ICOS does not require an on-axis alignment, having the mechanical and optical center of the cavity coaligned is not a requirement as long as the mirrors are nearly parallel. This means that it is not necessary to have the ability to tilt the mirrors, thus eliminating the need for adjustable mirror mounts as well as bellows in the cavity. This is important for the flow characteristics of the system as it eliminates dead volume and also minimizes the surface area in the cavity. The light, leaving the cavity through the back of the rear mirror, is focused by a 10 cm ZnSe lens (ISP Optics) onto a 3 mm diameter MCT detector (Kolmar Technologies) with an 8 mm diameter F-1 germanium meniscus (Janus) in front of it. The detector is housed in a 0.75 L LN₂ dewar to maximize sensitivity.

The optical cavity is aligned using an empirical method. The goal in alignment is to minimize the optical noise within the system while maintaining an adequate signal-to-noise ratio. This is measured by calculating the noise at each point along the ICOS spectrum. By looking at the average per point noise along a section of the scan with no absorption features, a robust number with which to evaluate the magnitude of noise in our signal is obtained. The alignment procedure then becomes one of minimizing the per point noise, which is accomplished by using the two front alignment mirrors, which give enough degrees of freedom to control the

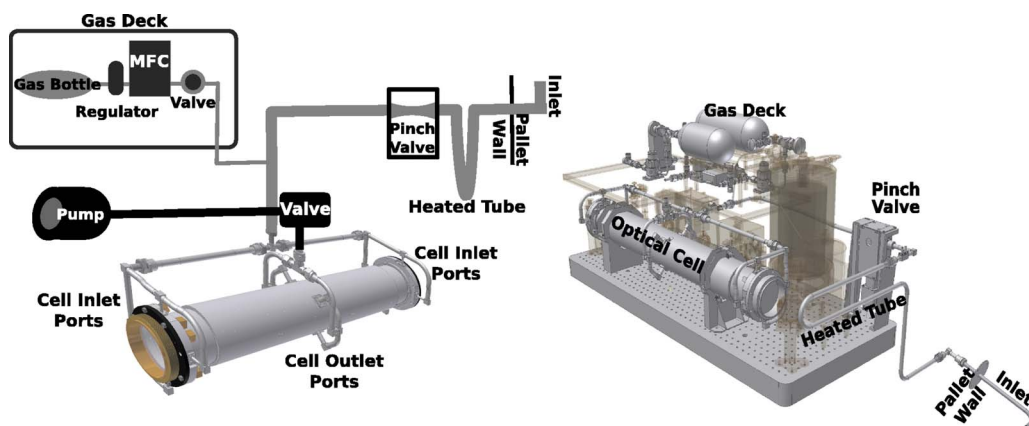


FIG. 5. (Color online) Schematic (left) and drawing (right) of the major components of the ICOS flow system. Details are discussed in the text.

position and angle at which the laser beam enters the optical cavity.

B. Flow system

The flow system includes the components necessary to bring ambient air into the optical cell as well as an in-flight gas addition system used for calibration. In designing the flow system there are three major goals that need to be addressed:

- (1) minimizing the residence time of air in the cell;
- (2) maintaining a constant pressure and temperature in the cell; and
- (3) minimizing contamination of the air from dead volumes and surfaces.

The flow system of the ICOS instrument is shown in Fig. 5. Flow through the system is maintained by an oil-less scroll pump (Varian TriScroll 600 dry pump) located at the outlet end of the flow system, which at full speed displaces 8.3 l/s. Given the volume of the cell, this produces a residence time of 0.86 s. Ambient air is brought into the system through a rear facing inlet for particle rejection and which protrudes 41 cm from the side of the pallet. The inlet is heated to ensure that water vapor does not condense in the inlet. After the air passes through the inlet, it flows through a heated section of tube in order to raise the temperature of the air sample to near 25 °C, which is the temperature of the optical rack enclosure. It is important that the air entering the optical cavity is at a constant uniform temperature, as temperature gradients will lead to increased uncertainty in the concentration of gas species. This is especially true for the measurement of H₂O as the absorption cross-sections have a large temperature dependence due to choosing a high *J*-state line for H₂O. This was done in order to have comparable absorption depths with the less abundant isotopologues. A 1° uncertainty in temperature leads to a 0.25% uncertainty in the concentration of H₂O. Temperature gradients within the optical cavity were measured in the laboratory using multiple 1 MΩ thermistors placed inside the cavity as well as on the surface. The maximum gradient measured under flight flow conditions was 0.5 °C.

A pinch valve (Swagelok, part SS-A3STBM8; modified) is used to regulate the cell pressure at 53 hPa (40 torr). The valve consists of a 1 cm i.d. Viton tube that is compressed by a stepper motor actuated plunger to restrict the flow. The pinch tube element allows for high conductance without dead volume (the pinch element has a smooth inner bore). A proportional-integral feedback loop between the cell pressure and stepper motor position maintains a constant cell pressure as the ambient pressure changes. The pinch valve is connected to the optical cell by 70 cm of 1.25 cm o.d. stainless steel tubing. The optical cell is a 10 cm diameter aluminum tube that is 90.57 cm long, and the ends are capped by the high-reflectivity mirrors. To eliminate dead volumes or stationary eddies in the cell, the air is injected through four small ports spaced at 90° on a flange at each end of the cell. The ports are aligned so that the air will swirl around, eliminating dead volumes at the edges of the mirrors. The air leaves the cell through four exit ports located in the middle of the cell, which are connected via tubing to the scroll pump.

To minimize contamination from water on the walls of the cell and input tubes, all surfaces are coated with a hydrophobic fluoropolymer (Cytonics, FluoroPel). Additionally, all connections along the input tubing are made using VCO-B (Swagelok) fittings that use an L-ring seal to reduce surface area and dead volumes at connection junctions, which have the potential to trap water. The system is also purged with dry air before flight, and the cell is then sealed via the pinch valve on the input end and a solenoid valve (BOC Edwards, part C41752200) located between the cell and the pump. The cell remains closed until after takeoff and the aircraft has reached a designated altitude, typically around 5 km depending on cloud layers.

The ICOS instrument is equipped with a gas deck that consists of two high pressure gas bottles capable of delivering dry air or air with a small amount of water and methane to the cell. The gas deck is contained within the optical thermal enclosure to ensure that the gas is at the same temperature as the optical cavity. The first gas bottle is a 1 L bottle filled to typically 2200 psi with ultrapure dry air with less than 0.2 ppmv of water (Scott Marrin). The second gas bottle is a 0.75 L bottle typically filled to 1500 psi with air contain-

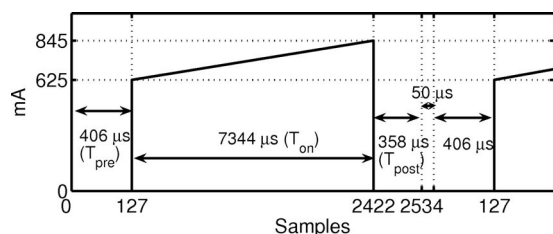


FIG. 6. Timing diagram of an ICOS waveform. A zero is recorded before (T_{pre}) and after (T_{post}) each spectrum. The laser is on for 7344 μs during which time the current is ramped from 625 to 845 mA. Between scans there is a 50 μs period when the QCLI resets and the data are processed by the CPCI computer.

ing about 20 ppmv of water vapor and about 5 ppmv of methane. The gas bottles are connected to MKS1709 mass flow controllers (MFCs). Each MFC has a solenoid valve (Saint-Gobain, Furon DVX) in front of it in order to provide a positive shutoff, as MFCs often leak small amounts of gas even when in the off position. The gas deck is connected to the main flow tube via an 8 mm o.d. stainless steel tube that intersects with the main flow tube just before the cell.

The ICOS instrument contains a separate flow system for regulating the pressure of the laser and detector LN2 dewars. Maintaining a constant dewar pressure for the laser is important because changes in dewar pressure lead to changes in the temperature of the QCL, which in turn change the tuning range of the laser. A pressure sensor (Pressure Systems, part 30-431-10015) is located at the top of the laser dewar. The two dewars are connected via 8 mm tubing and this tubing is connected to a three-way solenoid valve and a MFC. When instrument power is off, the three-way valve is open to the atmosphere. When power is on, the three-way valve is switched to the MFC, and the pressure is maintained at 1027 ± 1 hPa using proportional-integral-derivative (PID) control software to control the MFC. The dewar pressure system also has burst disks to prevent accidental overpressuring of the dewars that could result in the dewars exploding.

C. Data acquisition

The QCLI driver generates the current waveforms that drive the QCL. It has a programmable frequency scan and scan rate, produces stable waveforms with low noise, and has safeguards that prevent over temperature and over current conditions. The QCLI provides two different types of waveforms: ICOS and ringdown. ICOS waveforms require almost continuous operation of the laser while ramping the control current in order to scan the frequency of the laser. Ringdown waveforms require the laser to be turned on and off quickly and to have the decay signal recorded at high temporal resolution. In order to acquire ringdown times at frequencies corresponding to the ICOS range, the ringdowns must be taken at different current levels. While these two waveforms are very different, they can both be generated by summing constant current and linear ramp outputs.

A typical waveform used in the ICOS system is shown in Fig. 6. The diagram shows the output current from the QCLI plotted versus sample number (i.e., samples recorded by the

computer). The current is ramped from 625 to 845 mA, which corresponds to approximately 1485.6 to 1483.7 cm^{-1} and takes 7344 μs , giving a tuning rate of 30 A/s or 260 cm^{-1}/s . In order to calculate an absorption depth, a zero needs to be measured as the ac coupled nature of the detector means that zero is not necessarily at 0 V. A zero is recorded at the beginning and end of each scan during laser off time. Following the waveform, which takes 8108 μs , there is a 50 μs period during which the system resets for the next waveform. This gives ICOS a total duty cycle of greater than 99% and a laser duty cycle of 90%. The spectra are recorded at a rate of about 120 Hz, and typically 120 spectra are coadded, resulting in a 1 Hz averaged data acquisition rate.

The ringdown waveform differs from the ICOS waveform mainly in the speed with which the laser needs to be switched on and off and the amount of data that are generated. The switching time for the QCLI, which is the time it takes the current supplied to the laser to drop to zero amperes, is 1 μs . This fast switching time is essential for using the cw-laser in ringdown mode. Due to the larger amount of data generated, ringdowns are fit in real time, as described in the next section, and only the τ of the ringdown is recorded. Some of the raw ringdowns are saved as a postflight check of the ringdown fitting algorithm. In order to make sure that the cavity time constant is in fact constant across the scan, the current at which ringdowns are taken is ramped over a similar range of current to the ICOS waveform.

The noise output of the QCLI is low enough to avoid any significant lineshape perturbations, as noise on the output current of the QCLI leads to multiple frequencies of light for a nominal current level. This results in an apparent broadening of the absorption lines and a reduction in the peak absorption depth. For the QCLI the noise specification is $\Delta I = 50 \mu\text{A}$ rms or 200 μA peak-to-peak. A current noise of 50 μA rms corresponds to about $4 \times 10^{-4} \text{cm}^{-1}$ or 10% of the Doppler full-width at half-maximum.

The QCLI communicates with the data acquisition system, a compact PCI (CPCI) computer via a trigger pulse that synchronizes the timing of data acquisition with that of the ringdown laser pulses and ICOS ramps. The detector analog bandwidth is 500 kHz. The signal is then filtered using a sixth order Bessel filter, which has a linear phase shift and constant delay at all frequencies of interest. The data are then sampled at 1 MHz by the analog to digital converter (A/D) card on the CPCI and coadded as described above before being recorded on a flash disk.

IV. DATA ANALYSIS AND SPECTRAL FITTING ALGORITHM

The concentration of a species in molecules/ cm^3 is related to the absorption depth α via the physical relationship

$$\alpha(\nu) = [\text{molecules}/\text{cm}^3] \frac{S_{\eta\eta'} L}{\sqrt{\pi/\ln(2)} \gamma_d} K(\nu, \nu_{\eta\eta'}, \gamma_L/\gamma_d), \quad (11)$$

where $S_{\eta\eta'}$ is the spectral line intensity for a transition between states η and η' in $\text{cm}^{-1}/(\text{molecules cm}^{-2})$, L is the length of the optical cavity in centimeter, γ_d and γ_L are the

Doppler and Lorentzian half-widths at half maximum (HWHM), respectively, and K is the Voigt lineshape function. The Voigt lineshape function K is given by an empirical algorithm that calculates the convolution of the Gaussian and Lorentzian lineshapes (i.e., the Voigt lineshape).^{32,33} The accuracy of ICOS depends on how well the absorption line can be fit to Eq. (11) and how accurately $S_{\eta\eta'}$ is known. Most of the spectroscopic line parameters are taken from the HITRAN database.³⁴ However, due to the importance of $S_{\eta\eta'}$, the temperature dependent line intensities and the pressure and temperature dependent line widths are measured in our laboratory as described in the next section.

The temperature dependence of the line intensity is calculated using the HITRAN parameters in the equation

$$S_{\eta\eta'}(T) = S_{\eta\eta'}(T_{\text{ref}}) \frac{Q(T_{\text{ref}})}{Q(T)} \frac{\exp(-c_2 E_{\eta}/T)}{\exp(-c_2 E_{\eta}/T_{\text{ref}})} \frac{[1 - \exp(-c_2 \nu_{\eta\eta'}/T)]}{[1 - \exp(-c_2 \nu_{\eta\eta'}/T_{\text{ref}})]}, \quad (12)$$

where T is the temperature of the gas being measured, T_{ref} is the reference temperature at which the line intensity is defined (typically 296 K), c_2 is the second radiation constant (hc/k), $Q(T)$ is the total internal partition sum, and E_{η} is the lower state energy. The temperature of the gas is measured in the optical cavity with two 1 M Ω thermistors that have an accuracy of 0.1 K.

The pressure broadened half-width (i.e., Lorentzian half-width) γ_L for a gas at pressure p and temperature T is given by

$$\gamma_L(p, T) = \left(\frac{T_{\text{ref}}}{T}\right)^n \gamma_{\text{air}} p, \quad (13)$$

where n is the coefficient of temperature dependence of the air-broadened half-width and γ_{air} is the air-broadened half-width. We ignore the effect of self-broadening on the Lorentzian width, as the partial pressure of the molecules that are being measured is very small compared to the total pressure. There is also a small dependence of the transition frequency on pressure given by

$$\nu_{\eta\eta'}^* = \nu_{\eta\eta'} + \delta_{\text{air}} p, \quad (14)$$

where δ_{air} is air-broadened pressure shift. The Doppler half-width is given by

$$\gamma_D = \nu_{\eta\eta'} \sqrt{\frac{2kT \ln(2)}{mc^2}}, \quad (15)$$

where k is Boltzmann's constant, m is the mass of the molecule, and c is the speed of light.

The lineshapes in the ICOS spectra are modified because of the skewing effect described previously. Therefore, in order to obtain α , the absorption spectra must be fit to Eq. (6), which defines the intensity of light transmitted through the cavity. For the purposes of fitting, Eq. (6) can be represented as a matrix where each term in the matrix represents the intensity of light at a particular frequency and particular time within the cavity. The power at a particular frequency in the cavity P_{ν} decreases over time as photons are lost through the mirrors and due to molecular absorption. The fractional loss per unit time τ^* is defined as

$$\tau^* = \exp(-dt/\tau), \quad (16)$$

where τ is defined as in Eq. (3) and is dependent on the mirror reflectivity and intracavity molecular absorption. While the mirror reflectivity is typically constant during a flight, possible changes can occur due to contamination of the mirrors. As a result, the reflectivity of the mirrors is measured using a ringdown scan when no absorber is present in the cavity. The ringdowns are fit with a linear-linear fitting algorithm. In this algorithm a line is fit to y versus y shifted by 20 samples. The slope of the line is $\exp(ndt/\tau)$ where n is the number of samples shifted and dt is the sample period. The advantage of this fitting algorithm is that it does not require a knowledge of zero, which is advantageous when using a detector that is ac coupled. In simulations this method compares well with a nonlinear least-squares fitting approach and performs better than a log-linear approach in addition to being much faster.

We can write the summation of Eq. (6) over all frequencies present in the cavity as the matrix

$$\begin{matrix} P_{\nu_1} & P_{\nu_1} \tau_{\nu_1}^* & P_{\nu_1} \tau_{\nu_1}^{*2} & P_{\nu_1} \tau_{\nu_1}^{*3} & P_{\nu_1} \tau_{\nu_1}^{*4} & \cdots \\ 0 & P_{\nu_2} & P_{\nu_2} \tau_{\nu_2}^* & P_{\nu_2} \tau_{\nu_2}^{*2} & P_{\nu_2} \tau_{\nu_2}^{*3} & \\ 0 & 0 & P_{\nu_3} & P_{\nu_3} \tau_{\nu_3}^* & P_{\nu_3} \tau_{\nu_3}^{*2} & \\ 0 & 0 & 0 & P_{\nu_4} & P_{\nu_4} \tau_{\nu_4}^* & \\ \vdots & & & & & \ddots \end{matrix} \quad (17)$$

Each row represents the time evolution of a particular frequency, and the sum of each column represents the total power within the cavity at a particular time from all frequencies. The baseline power P_{ν} was initially fit using a cubic polynomial to approximate the baseline. While this is adequate for strong absorption features, as the signal-to-noise ratio approaches one, small perturbations in the baseline can cause biases in the retrieved data. In the ICOS spectra, these perturbations are caused by interference fringes or etalons between extracavity optics and between the cavity mirrors and also from oscillations in the laser power curve. The cavity etalons have been reduced using off-axis alignment in combination with rapid scanning of the laser. While the cavity etalons are still present, they have frequencies much higher than a typical line width and do not affect the data. However, the periods of the extracavity etalons are comparable to the line width of an absorption feature and therefore are capable of generating biases in the extracted concentration and thus must be accounted for in order to minimize errors.

An example of how an etalon can cause a bias in the retrieved concentration of a weak absorption feature is shown in Fig. 7. The two sets of plots on the left show the data in red and the fit to the data in green. The residual (data minus fit) is shown above each plot. The top plot is fit using a cubic polynomial to represent the baseline. The etalon is clearly visible above the noise and has a magnitude of ± 7 as compared to the strong line which has a depth of 25. The etalon represents 25% of the peak magnitude of the strong line on the right. However, the usable portion of the absorption feature, or the portion of the absorption feature that is

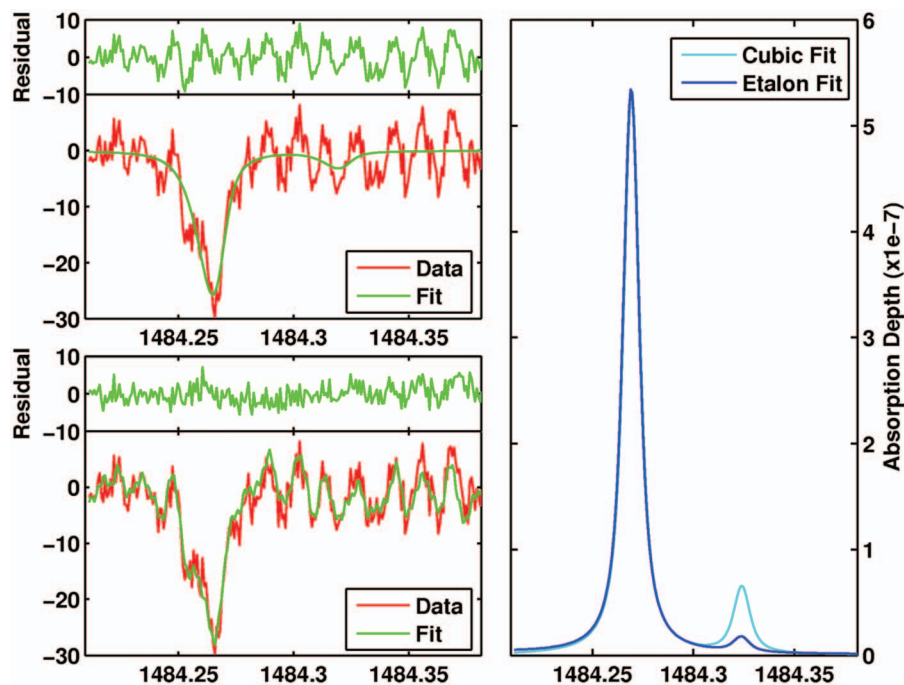


FIG. 7. (Color) Line fitting using two types of baselines. The two sets of plots on the left show the data in red and the fit to the data in green. The residual (data minus fit) is shown above each plot. The top plot is fit using a cubic polynomial to represent the baseline. The bottom plot shows the same data fit using a baseline composed of a cubic polynomial and frequencies that represent the dominant etalon modes of the spectrum. In order to allow for random phase, each etalon is modeled as the sum of a sine and cosine. The right hand plot shows the absorption coefficient α as calculated by the cubic and etalon fits in cyan and blue, respectively.

above the noise, spans multiple etalons, and therefore the errors are much smaller than the magnitude of the residual would imply. For the weak absorption on the left, the opposite is true. The usable portion of the absorption feature only spans one period of the etalon, and the magnitude of the etalon is twice that of the line. The bottom plot shows the same data fit using a baseline composed of a cubic polynomial and frequencies that represent the dominant etalon modes of the spectrum. In order to allow for random phase, each etalon is modeled as the sum of a sine and cosine. The etalon fit reproduces the oscillations in the baseline as can be seen by comparing the residuals. The right hand plot shows the absorbance α as calculated by the cubic and etalon fits in cyan and blue, respectively. Fitting the etalon does not change the fit of the stronger line as α is the same for both fits. However, the magnitude of the weaker line was mostly due to the etalon.

In summary, the fitting algorithm fits the data to Eq. (6) where an empirically defined basis set is used to represent the baseline power curve, R is measured by ringdown, and α is defined by Eq. (11). The magnitude of α is directly proportional to concentration, and the shape is given by an empirical algorithm for calculating the Voigt lineshape. The engine of the fitting algorithm uses the Levenberg–Marquardt method from Numerical Recipes in C,³⁵ modified for C++, and with the ability to dynamically fix and float parameters. By default, the concentration and baseline are the only floating parameters. Optionally, the Lorentzian and Doppler line-widths and the position of the line can be floated.

An example of fitting data from the CR-AVE science mission is shown in Figs. 8–10. The spectra are first fit with a polynomial to approximate the baseline power curve. In the case of the representative spectrum shown in Fig. 8, the polynomial is fourth order. The raw data, the fit to the data, and the baseline are shown in the top plot in blue, green, and red, respectively. The second plot shows the data and fit with

the baseline removed (top two lines, marked 4p0e, which denotes the order of the polynomial and the number of additional frequencies added). The residual is shown in the third plot marked 4p0e. It is evident that the fourth order polynomial is not sufficient to represent the baseline, as several oscillations from etalons and other artifacts can be seen in the residual. These oscillations will be represented in the

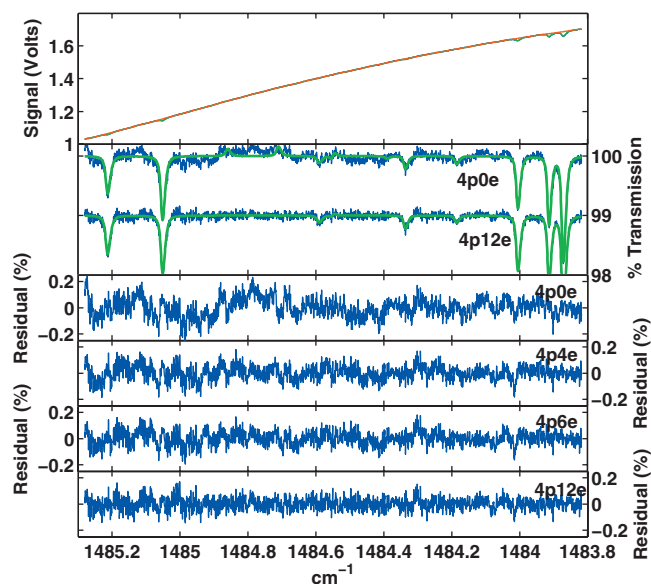


FIG. 8. (Color) Fits of data at 4 ppm H_2O for spectra taken during the CR-AVE mission. Top plot shows the raw data, the fit to the data, and the baseline in blue, green, and red, respectively. Plots in the next panel show the baseline removed from the data with the data plotted in units of percent transmission in blue and the fit to the data in green. Two different baseline fits are shown. The first uses just a fourth order polynomial, marked 4p0e, and the second uses a fourth order polynomial and 12 frequencies to represent oscillations in the baseline, marked 4p12e (see text for details). The second fit is offset by 1% for visual clarity. The bottom four plots show the residuals from the fit in the same units as the second plot. The residuals are from four different baseline representations as discussed in the text.

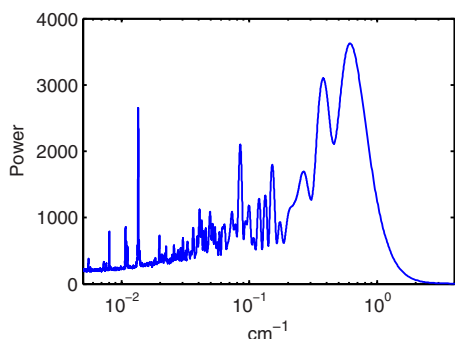


FIG. 9. (Color online) DFT of the residuals from a fit using a fourth order polynomial to represent the baseline. Shown is the average of all the DFTs from the data plotted in Fig. 10.

baseline using sine and cosine waves as previously discussed. In order to choose the frequencies to include, a discrete Fourier transform (DFT) is performed on the residuals of the fits. Shown in Fig. 9 is the mean of all the DFTs for a section of data. The baseline is then composed of the fourth order polynomial and a combination of the most prominent frequencies. Figure 8 shows the residuals from baselines with zero, four, six, or 12 frequencies added and are marked 4p0e, 4p4e, 4p6e, and 4p12e, respectively. Figure 10 shows the derived mixing ratio of water vapor (top plot) and HDO (bottom plot) using the four different baselines described above. The largest changes in mixing ratio come from adding four or six frequencies, even though the residuals of the four and six fit are not significantly different. The difference in H_2O or HDO mixing ratio between the six and 12 frequency baselines is negligible, even though the residual from the baseline with 12 frequencies has the smallest standard deviation. The 12 frequency baseline therefore is an acceptable representation of the baseline as the residual is small and does not have any prominent nonwhite components. Since the absorption depth of HDO is weaker than H_2O , the effect of accounting for the oscillations in the baseline is larger for HDO. However, for both the maximum change from a poor fit (4p0e) to a good fit (4p12e) is only 0.3 ppmv and 0.2 ppbv for H_2O or HDO, respectively.

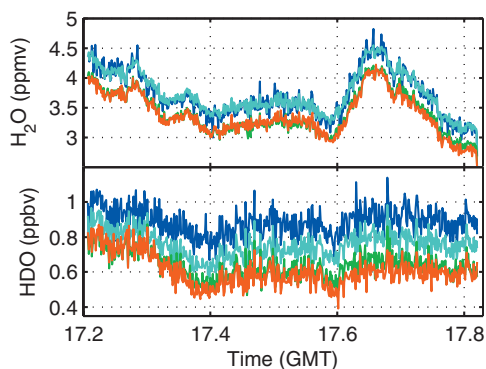


FIG. 10. (Color) Top plot shows the water vapor mixing ratio derived from spectra using four different baselines that have a different number of sine waves added to represent etalons and other artifacts in the baseline power curve. The baselines all use a fourth order polynomial but have either zero, four, six, or 12 frequencies added and are plotted in blue, cyan, green, and red, respectively. The bottom plot shows the HDO mixing ratio derived from the same spectra as in the top plot.

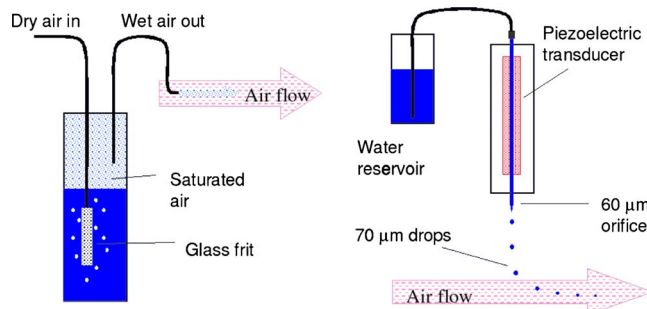


FIG. 11. (Color online) Schematic of the two types of water addition systems used to calibrate ICOS. The bubbler system is shown on the left and the microdroplet injector is shown on the right.

V. CALIBRATION OF THE ICOS INSTRUMENT

Calibration of the ICOS instrument in the laboratory is performed by injecting known quantities of water vapor, with known isotopic composition, into the instrument and checking that the fitting algorithm yields correct mixing ratios. The ultimate accuracy of the ICOS instrument is dependent on how well the amount of water vapor added can be quantified. To minimize uncertainties, the calibrations are performed using two different water addition systems: a bubbler system and a microdroplet injector system (Fig. 11). Both techniques have been checked by measuring the concentration using the absorption of Lyman- α radiation at 121.6 nm, whose cross-section has been accurately determined.^{36,37}

The first, a bubbler system, mixes saturated air and a dry carrier gas to create a carrier gas with known water vapor mixing ratios in the range of 0 to 200 ppmv (Fig. 12). The carrier gas is either zero air (IGOS) that is further dried using a column of molecular sieves ($[\text{H}_2\text{O}] < 3$ ppmv) or nitrogen gas from a LN2 tank ($[\text{H}_2\text{O}] \approx 0.2$ ppmv). The main carrier gas flow is set using a 1 kg/s (100 slm) (slm denotes standard liters per minute) MFC (MKS Instruments) and is regulated to maintain a 53 hPa (40 torr) pressure in the optical cavity. Air that is saturated with water vapor is added using either 0.1 or 1 g/s (10 or 100 SCCM) (SCCM denotes standard

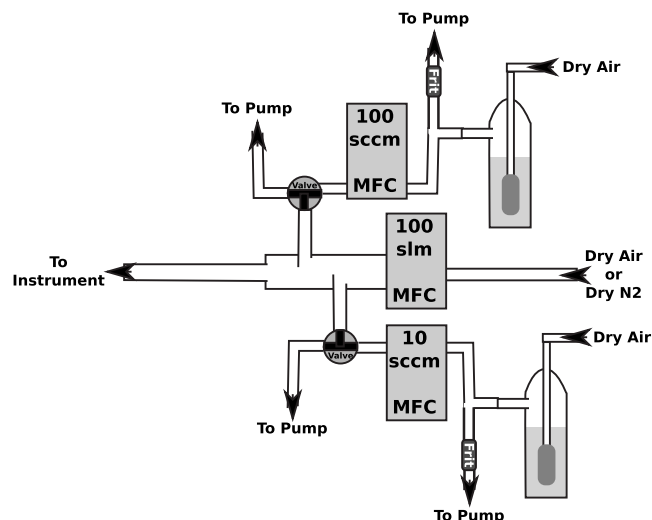


FIG. 12. Schematic of the bubbler system. Dry air or nitrogen is mixed with saturated air to create air with a known water vapor mixing ratio. Details of the system are discussed in the text.

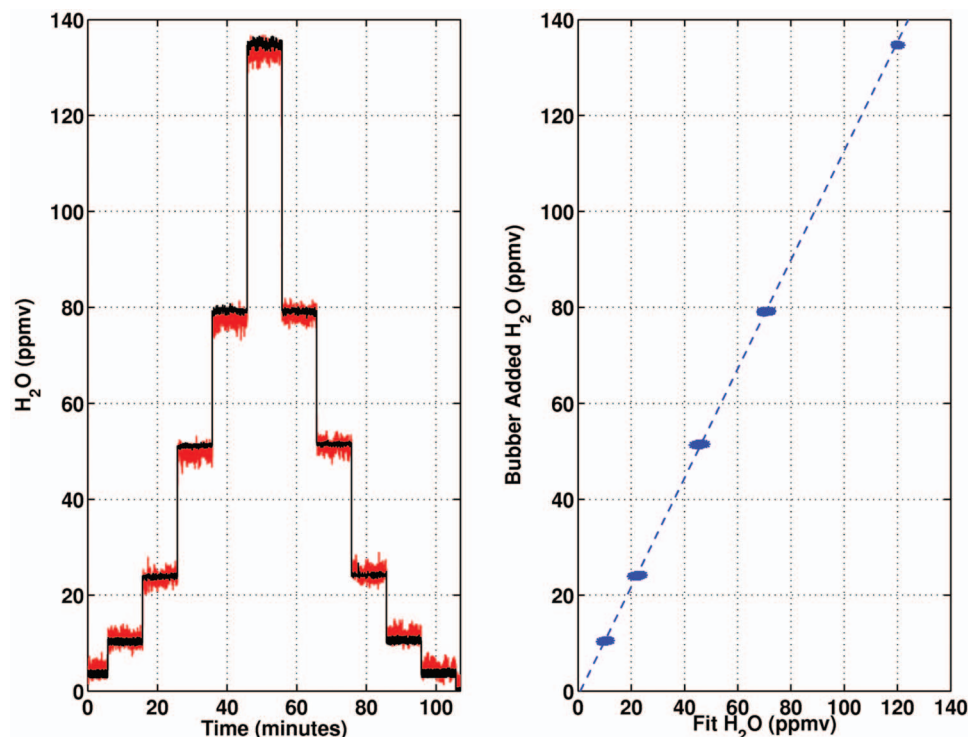


FIG. 13. (Color) Calibration run using the bubbler system. The plot on the left shows the mixing ratio of water added to the system calculated from the bubbler and the mixing ratio calculated from the fit in black and red, respectively. The plot on the right shows the water vapor added via the bubbler plotted vs the water vapor calculated from the fit. The slope of the line is the correction to the HITRAN absorption cross-sections.

cubic centimeter per minute at STP) MFCs, depending on the final mixing ratio that is desired. The saturated air is generated by passing dry air through a single-stage bubbler, which uses a glass frit to release the air through liquid water (detail on left side of Fig. 11). The water saturation mixing ratio and the isotopic composition above the liquid water depend on the temperature and pressure, which are continually measured.^{38,39} The isotopic composition of the bulk calibration water was determined by averaging the results from three stable isotope laboratories (University of Idaho, Boston University, and University of Colorado). To minimize hysteresis effects from pressure changes in the bubbler caused by changes in the flow rate, a 2 g/s (200 SCCM) frit is placed between the bubbler and a pump, reducing the maximum pressure change to 30% when the flow controller is fully open. To minimize hysteresis effects from the warm-up time of the flow controllers, a three-way valve is used between the flow controller, a pump, and the instrument. This allows the flow controller to be on even though the saturated air is not being added to the carrier gas. In addition, the valve acts as a quick and positive shutoff for the flow controller. The accuracy of the bubbler system is dependent on measuring the pressure and temperature of the bubbler, accounting for fractionation during evaporation, and the uncertainties of the flow controllers.

The second approach uses a microdroplet injector (Microdrop, part MD-K-130-010) to generate unsaturated air with a known water vapor mixing ratio (detail on right side of Fig. 11). Water from a reservoir is emitted from a 60 μm opening to produce 70 μm droplets, which evaporate in the dry carrier gas. The mass of water added is determined by the droplet size and the frequency of the droplets. Since the entire droplet is evaporated into unsaturated air, no fraction-

ation takes place. The uncertainties in this technique are determined from the ability to measure the mass and number of droplets.

A calibration run consists of using one of the water addition systems to vary the mixing ratio of water in the ICOS optical cavity and comparing the calculated concentration to the concentration determined by fitting the absorption spectra. Figure 13 shows an example of a calibration run. The left plot shows the amount of water vapor added by the bubbler in black. The water vapor mixing ratio calculated from the fit to the data is plotted in red. The difference is due to a combination of (i) errors in the HITRAN database, (ii) uncertainties in the instrument function such as distortion of absorption features due to current noise, and (iii) nonwhite components in the baseline noise. Errors in the water source are minimized using the redundant water addition techniques and comparisons with other measurement techniques (discussed below). The slope between the fitted concentrations and the concentrations as calculated from the water addition system yield the modification to the HITRAN absorption cross-sections. Modification in the HITRAN air-broadened line widths γ_{air} is determined by titration at different pressures. For each absorption line the data are fit to Eq. (13) to obtain a best fit for γ_{air} . To ensure that there are no dependencies on concentration, the pressure titration is performed at different mixing ratios. Table I lists the spectroscopic parameters used in the ICOS fitting program. Parameters that have been changed from the values listed in HITRAN are shown in italics and are within 10% of the HITRAN values.

Table II lists the relevant uncertainties for H₂O, H₂¹⁸O, and HDO as well as δD and $\delta^{18}\text{O}$. The first column gives the average wintertime tropical stratospheric value of each species. Precision is derived directly from the measurement it-

TABLE I. Spectroscopic line parameters from the HITRAN database. Line intensities and air broadening widths have been corrected as described in the text, and the values that have been changed appear in italics.

Molec.	Iso ^a	ν ^b	S ^c	γ_{air} ^d	E ^e	n_{air} ^f	δ_{air} ^g
CH ₄	61	1483.7922	<i>3.609E-22</i>	<i>0.0696</i>	157.1	0.75	-0.002
CH ₄	61	1483.8344	<i>2.267E-22</i>	<i>0.0589</i>	157.1	0.75	-0.002
H ₂ ¹⁸ O	12	1483.9260	<i>8.391E-23</i>	<i>0.0694</i>	550.5	0.64	-0.003
HDO	14	1484.0128	3.619E-25	0.0920	221.9	0.69	-0.002
HDO	14	1484.1064	<i>2.324E-23</i>	<i>0.0856</i>	225.9	0.64	-0.002
H ₂ O	11	1484.2570	<i>1.779E-23</i>	<i>0.0691</i>	1899.0	0.41	-0.005
HDO	14	1484.3118	3.534E-24	0.0846	233.0	0.73	0.001
HDO	14	1484.4701	3.534E-24	0.0846	233.1	0.73	-0.003
HDO	14	1484.4708	6.455E-25	0.0829	964.9	0.45	0.003
H ₂ O	11	1484.5048	1.065E-25	0.0629	3659.9	0.41	0.002
H ₂ ¹⁷ O	13	1484.5109	1.973E-23	0.0953	205.5	0.77	-0.001
HDO	14	1484.6310	3.038E-24	0.0879	520.1	0.59	-0.001
H ₂ ¹⁷ O	13	1484.7805	2.166E-24	0.0836	781.4	0.59	0.003
H ₂ ¹⁸ O	12	1484.9715	<i>1.021E-22</i>	<i>0.0831</i>	325.2	0.69	-0.006
H ₂ O	11	1485.1336	<i>6.253E-23</i>	<i>0.0866</i>	1907.6	0.77	-0.001

^aHITRAN molecule number and isotope number.^bLine position in wave numbers (cm⁻¹).^cIntensity in cm⁻¹/(molecule cm⁻²) at 296 K.^dAir-broadened half-width (HWHM) in cm⁻¹/atm at 296 K.^eLower state energy in cm⁻¹.^fCoefficient of temperature dependence of air-broadened half-width.^gAir-broadened pressure shift of line transition in cm⁻¹/atm at 296 K.

self and is the equivalent mixing ratio of a line with depth equal to the fit residual. This value is equivalent to the standard deviation of the data we would measure while sampling at constant mixing ratio. The laboratory accuracy is the accuracy of the bubbler system used to determine the spectral cross-sections and line widths. Finally the maximum bias uncertainty is the uncertainty due to oscillations in the spectrum baseline and other artifacts that might bias the data. The magnitude of the bias is equal to the equivalent mixing ratio of an absorption line whose depth equaled the magnitude of the baseline oscillation. This uncertainty is additive and is most significant at low mixing ratios as observed in the stratosphere. The bias can be either positive or negative and may change during the course of a flight and from day to day depending on alignment.

An additional source of uncertainty in flight comes from

TABLE II. Uncertainties for the water species measured by ICOS. The first column gives the average wintertime tropical stratospheric value of each species. Precision is determined by calculating the equivalent mixing ratio of a line with depth equal to the residual of the fit. This number gives the same result as calculating the standard deviation of the data during a period with constant mean mixing ratio. The laboratory accuracy is the accuracy of the spectral cross-sections and line widths determined by calibration. The maximum bias uncertainty is the uncertainty due to etalons in the spectrum baseline and other artifacts that bias the data.

Molec.	Ave. strat. value	Precision		Bias uncertainty
		[4 s(1- σ)]	Accuracy (lab)	
H ₂ O	3 ppmv	0.14 ppmv	5%	± 0.25 ppmv
H ₂ ¹⁸ O	5 ppbv	0.16 ppbv	5%	± 0.3 ppbv
HDO	0.5 ppbv	0.10 ppbv	5%	± 0.06 ppbv
δD	-450‰	50‰	5%	± 100 ‰
$\delta^{18}O$	-75‰	30‰	5%	± 50 ‰

contamination from water desorption from the walls of the cavity. This uncertainty is time dependent and is hard to quantify without comparison with another water instrument. A time constant for water desorption can be evaluated in the laboratory by comparing ICOS to an instrument in which contamination from detection axis walls is insignificant, such as the Lyman- α photofragmentation instrument.⁴⁰ Since Lyman- α is insensitive to water desorption from the walls at the detection axis, any contamination observed will be due to water on the tubing between the bubbler system and instrument inlets. Additional contamination observed in the ICOS instrument is therefore due to desorption from the ICOS inlet tubing and cell walls. Figure 14 shows two such comparisons. The first is the time it takes for the difference between ICOS and Lyman- α to reach zero after a pulse of high water and the second is after 20 min of continuous flow of high water. Even after 20 min of high water, contamination is only 0.5 ppmv after 4 min and less than 0.1 ppmv after 20 min.

Present work in the laboratory is centered on eliminating or at least minimizing the uncertainties discussed and identifying the effects on mixing ratio and δD . Cross-calibration with other instruments both in the laboratory and in flight helps to validate the uncertainties listed above and to identify systematic errors and unpredicted problems. ICOS has undergone cross-calibrations in the laboratory with Harvard Ly- α water and HOxotope,⁴¹ an isotope instrument using a fundamentally different technique for isotopic detection from that of ICOS. This multifaceted approach to calibration minimizes uncertainties and most importantly identifies errors caused by problems with the water addition system. ICOS has also participated in a water vapor and water isotope intercomparison campaign, AVE-WIIF, and agreed within 10% with the other instruments.⁴¹ These flight comparisons are

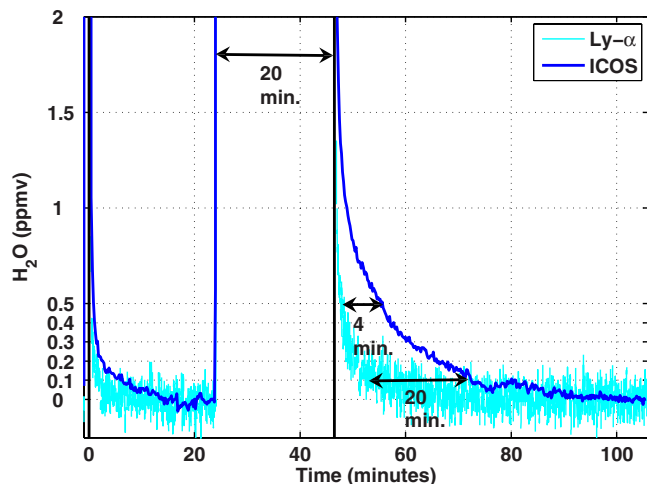


FIG. 14. (Color online) Time evolution of contamination from water desorbing off the ICOS cell and inlet tubing walls. High water added during a pulse and during a 20 min continuous flow. Residual contamination is observed by comparing water vapor mixing ratio measured by the Lyman- α instrument and by ICOS.

important for validating that the uncertainties measured in the laboratory are the same as in the flight environment.

VI. CONCLUSIONS

The Harvard ICOS instrument has flown successfully during four separate field campaigns starting during the winter of 2004–2005. It has demonstrated that the ICOS technique is not only robust enough to be used in a flight instrument but also sensitive enough to provide accurate concentrations of trace species, specifically the four primary isotopologues of water at stratospheric concentrations. ICOS is able to measure gas species in the ppbv and pptv ranges by employing an optical cavity to create an effective path length of 4.5 km in a 90 cm cell. Off-axis alignment allows ICOS to use a passive cavity without the requirement of locking the laser to the cavity modes. Due to the low transmission through the cavity mirrors, a high powered QCL (30 mW) is used to provide a cw-laser source.

Extensive calibrations and validations are performed in the laboratory and in flight in order to ensure that ICOS is reporting accurate concentrations. Calibration in the laboratory use two different water addition systems as well as cross-calibration with other instruments to validate the fitting algorithm used to retrieve concentrations from absorption spectra. Validation during field campaigns is performed by comparisons with other instruments during flight. Both of these have shown that the limiting uncertainty in the reporting of accurate concentrations at low signal to noise is the treatment of baseline artifacts and more advanced fitting algorithms are currently being developed to account for these artifacts. Biases for H_2O , HDO, and H_2^{18}O are less than 0.25 ppmv, 0.06 ppbv, and 0.3 ppbv, respectively. The accuracy of the laboratory calibrations yields uncertainties of 5% in the mixing ratios of all species, ignoring the additional uncertainty from the biases at low concentrations. The Harvard ICOS instrument has demonstrated a precision of 0.14 ppmv, 0.10 ppbv, and 0.16 ppbv in 4 s averages for H_2O , HDO, and

H_2^{18}O , respectively. At a water vapor mixing ratio of 5 ppmv the isotopologue ratio precision is 50‰ and 30‰ for δD and $\delta^{18}\text{O}$, respectively.

- ¹V. L. Dvortsov and S. Solomon, *J. Geophys. Res., [Atmos.]* **106**, 7505 (2001).
- ²D. B. Kirk-Davidoff, E. J. Hintsa, J. G. Anderson, and D. W. Keith, *Nature (London)* **402**, 399 (1999).
- ³C. A. Smith, J. D. Haigh, and R. Toumi, *Geophys. Res. Lett.* **28**, 179 (2001).
- ⁴J. Fasullo and D. Z. Sun, *J. Clim.* **14**, 2798 (2001).
- ⁵K. Minschwaner and A. E. Dessler, *J. Clim.* **17**, 1272 (2004).
- ⁶G. L. Stephens, S. C. Tsay, P. W. Stackhouse, and P. J. Flatau, *J. Atmos. Sci.* **47**, 1742 (1990).
- ⁷G. L. Stephens, D. G. Vane, R. J. Boain, G. G. Mace, K. Sassen, Z. E. Wang, A. J. Illingworth, E. J. O'Connor, W. B. Rossow, S. L. Durden, S. D. Miller, A. T. Austin, A. Benedetti, and C. Mitrescu, *Bull. Am. Meteorol. Soc.* **83**, 1771 (2002).
- ⁸J. R. Holton, P. H. Haynes, M. E. McIntyre, A. R. Douglass, R. B. Rood, and L. Pfister, *Rev. Geophys.* **33**, 403 (1995).
- ⁹J. R. Holton and A. Gettelman, *Geophys. Res. Lett.* **28**, 2799 (2001).
- ¹⁰E. F. Danielsen, *J. Geophys. Res., [Atmos.]* **98**, 8665 (1993).
- ¹¹S. C. Sherwood and A. E. Dessler, *Geophys. Res. Lett.* **27**, 2513 (2000).
- ¹²S. C. Sherwood and A. E. Dessler, *J. Atmos. Sci.* **58**, 765 (2001).
- ¹³R. Fu, Y. L. Hu, J. S. Wright, J. H. Jiang, R. E. Dickinson, M. X. Chen, M. Filipiak, W. G. Read, J. W. Waters, and D. L. Wu, *Proc. Natl. Acad. Sci. U.S.A.* **103**, 5664 (2006).
- ¹⁴T. F. Hanisco, E. J. Moyer, E. M. Weinstock, J. M. St Clair, D. S. Sayres, J. B. Smith, R. Lockwood, J. G. Anderson, A. E. Dessler, F. N. Keutsch, J. R. Spackman, W. G. Read, and T. P. Bui, *Geophys. Res. Lett.* **34**, L04814 (2007).
- ¹⁵E. Moyer, F. Irion, Y. Yung, and M. Gunson, *Geophys. Res. Lett.* **23**, 2385 (1996).
- ¹⁶D. Keith, *J. Geophys. Res., [Atmos.]* **105**, 15167 (2000).
- ¹⁷H. Craig, *Science* **133**, 1833 (1961).
- ¹⁸J. J. Scherer, J. B. Paul, A. O'Keefe, and R. J. Saykally, *Chem. Rev. (Washington, D.C.)* **97**, 25 (1997).
- ¹⁹A. O'Keefe, *Chem. Phys. Lett.* **293**, 331 (1998).
- ²⁰A. O'Keefe, J. Scherer, and J. Paul, *Chem. Phys. Lett.* **307**, 343 (1999).
- ²¹H. Barry, L. Corner, G. Hancock, R. Peverall, and G. Ritchie, *Chem. Phys. Lett.* **333**, 285 (2001).
- ²²J. J. Scherer, J. B. Paul, C. P. Collier, A. O'Keefe, D. J. Rakestraw, and R. J. Saykally, *Spectroscopy (Amsterdam)* **11**, 46 (1996).
- ²³D. Jackson, *Proc. R. Soc. London, Ser. A* **263**, 289 (1961).
- ²⁴G. S. Engel, W. S. Drisdell, F. N. Keutsch, E. J. Moyer, and J. G. Anderson, *Appl. Opt.* **45**, 9221 (2006).
- ²⁵J. Paul, L. Lapson, and J. Anderson, *Appl. Opt.* **40**, 4904 (2001).
- ²⁶A. Yariv, *Introduction to Optical Electronics*, 2nd ed. (Holt, Rinehart and Winston, New York, 1976).
- ²⁷E. J. Moyer, D. S. Sayres, G. S. Engel, J. M. S. Clair, F. N. Keutsch, N. T. Allen, J. H. Kroll, and J. G. Anderson, *Appl. Phys. B: Lasers Opt.* **92**, 467 (2008).
- ²⁸WB-57 high altitude research (<http://jsc-aircraft-ops.jsc.nasa.gov/wb57/index.html>).
- ²⁹Tropical composition, cloud and climate coupling (<http://www.espo.nasa.gov/tc4/>).
- ³⁰Aura validation experiment, Water instruments intercomparison flights (<http://www.espo.nasa.gov/ave-houston2/>).
- ³¹Costa Rica, Aura validation experiment (<http://www.espo.nasa.gov/ave-costarica2/>).
- ³²Y. Y. Liu, J. L. Lin, G. M. Huang, Y. Q. Guo, and C. X. Duan, *J. Opt. Soc. Am. B* **18**, 666 (2001).
- ³³Z. Shippony and W. G. Read, *J. Quant. Spectrosc. Radiat. Transf.* **78**, 255 (2003).
- ³⁴L. S. Rothman, D. Jacquemart, A. Barbe, D. C. Benner, M. Birk, L. R. Brown, M. R. Carleer, C. Chackerian, K. Chance, L. H. Coudert *et al.*, *J. Quant. Spectrosc. Radiat. Transf.* **96**, 139 (2005).
- ³⁵*Numerical Recipes in C*, edited by W. Press, S. Teukolsky, W. Vetterling, and B. Flannery, 2nd ed. (Cambridge University Press, New York, 1997).

³⁶B. Lewis, I. Vardavas, and J. Carver, *J. Geophys. Res.* **88**, 4935 (1983).

³⁷D. Kley, *J. Atmos. Chem.* **2**, 203 (1984).

³⁸D. Bolton, *Mon. Weather Rev.* **108**, 1046 (1980).

³⁹L. Merlivat and G. Nief, *Tellus* **19**, 122 (1967).

⁴⁰E. M. Weinstock, E. J. Hintsa, A. E. Dessler, J. F. Oliver, N. L. Hazen, J.

N. Demusz, N. T. Allen, L. B. Lapson, and J. G. Anderson, *Rev. Sci. Instrum.* **65**, 3544 (1994).

⁴¹J. M. St. Clair, T. F. Hanisco, E. M. Weinstock, E. J. Moyer, D. S. Sayres, F. N. Keutsch, J. H. Kroll, J. N. Demusz, N. T. Allen, J. B. Smith, J. R. Spackman, and J. G. Anderson, *Rev. Sci. Instrum.* **79**, 064101 (2008).